

Experimental classification of surface waves in optical coherence elastography.

Fernando Zvietcovich^{*a}, Jianing Yao^b, Jannick P. Rolland^b, Kevin J. Parker^a

^aDepartment of Electrical and Computer Engineering, University of Rochester, Rochester, NY, USA 14627; ^bThe Institute of Optics, University of Rochester, Rochester, NY, USA 14627

ABSTRACT

Various types of waves are produced when a harmonic force is applied to a semi-infinite half space elastic medium. In particular, surface waves are perturbations with transverse and longitudinal components of displacement that propagate in the boundary region at the surface of the elastic solid. Shear wave speed estimation is the standard for characterizing elastic properties of tissue in elastography; however, the penetration depth of Optical Coherence Tomography (OCT) is typically measured in millimeters constraining the measurement region of interest to be near the surface. Plane harmonic Rayleigh waves propagate in solid-vacuum interfaces while Scholte waves exist in solid-fluid interfaces. Theoretically, for an elastic solid with a Poisson's ratio close to 0.5, the ratio of the Rayleigh to shear wave speed is 95%, and 84% for the Scholte to shear wave. Our study demonstrates the evidence of Rayleigh waves propagating in the solid-air boundary of tissue-mimicking elastic phantoms. Sinusoidal tone-bursts of 400Hz and 1000 Hz were excited over the phantom by using a piezoelectric actuator. The wave propagation was detected with a phase-sensitive OCT system, and its speed was measured by tracking the most prominent peak of the tone in time and space. Similarly, this same experiment was repeated with a water interface. In order to obtain the shear wave speed in the material, mechanical compression tests were conducted in samples of the same phantom. A 93.9% Rayleigh-shear and 82.4% Scholte-Shear speed ratio were measured during experiments which are in agreement with theoretical results.

Keywords: Elastography, surface acoustic waves, Rayleigh waves, Scholte waves, optical coherence tomography.

1. INTRODUCTION

Elasticity is a fundamental biomechanical property measured in tissue since that provides important information related to the progression of pathologies. This information could lead to early diagnosis and improvement of treatment.¹ In the last 3 decades, different elastography techniques have been developed for several types of tissue to better diagnose and understand pathologies such as liver fibrosis², arteriosclerosis³, breast cancer⁴, glaucoma⁵, etc. For instance, ultrasound elastography (USE) is used to measure the biomechanical properties of tissue with a resolution and penetration depth on the order of 1mm, and 1cm, respectively.⁶ Magnetic resonance elastography (MRE), on the other hand, has a wider scanning range (approximately 1 cm – 10 cm) with resolutions on the order of ~10 mm.⁷ Optical coherence tomography (OCT) based elastography enables the acquisition of elasticity images ranging from 1 mm to 10 mm with micrometric resolution.⁸ Most elastography techniques enable elasticity estimation by determining the phase speed of shear waves propagating in tissue.⁹

Shear waves are a type of body wave that possess only a transverse component of movement, which means that the particle displacement produced by the wave in the medium is perpendicular to the direction of wave propagation. If certain properties in the medium such as Poisson's ratio and density are known under certain assumptions, the Young's modulus of the medium can be calculated using the phase speed of shear waves. Various types of waves are produced when a harmonic force is applied to a semi-infinite half space elastic medium.¹⁰ In particular, surface acoustic waves (SAW) are perturbations with transverse and longitudinal components of displacement that propagate in the boundary region at the surface of the elastic solid. Plane harmonic Rayleigh waves propagate in solid-vacuum interfaces while Scholte waves exist in solid-fluid interfaces.¹¹ Theoretically, for an elastic solid with a Poisson's ratio close to 0.5, the ratio of the Rayleigh to shear wave speed is 95%, and 84% for the Scholte to shear wave.^{11,12} Therefore, ignoring the presence of SAW and assuming shear wave propagation when the surface of the sample is mechanically excited will lead to the under-estimation of the phase speed, and, ultimately, to the miss-calculation of the Young's modulus of tissue¹³.

*fzvietco@ur.rochester.edu; phone 1 585 275-5069

Several investigations have been done measuring SAW speed in different types of tissue. In particular, Li, et al.¹⁴ estimated skin bulk mechanical properties by measuring SAW speed generated by a ring actuator and an OCT system. Similarly, Zhang, et al.¹⁵ demonstrated that the viscoelastic properties of skin calculated after measuring the phase speed of SAW can differentiate healthy skin from scleroderma using a scanning laser vibrometer. Zhang, et al.¹⁶ in other study measured speed of SAW for estimating the elasticity of lungs using ultrasound. Finally, the use of an air puff excitation to produce SAW in tissue was successfully achieved by Wang, et al.¹⁷ In their research, the depth-dependent phase velocity of Lamb waves was estimated in *ex vivo* rabbit cornea in order to distinguish four biomechanically distinct layers.

In this study, we aim to classify two types of SAW present in solid-air and solid-water interfaces using elastic tissue-mimicking phantoms and a phase-sensitive optical coherence tomography (PhS-OCT) system. The penetration depth of OCT is typically measured in millimeters constraining the measurement region of interest (ROI) to be near the surface. Phase speed of Rayleigh and Scholte waves are measured in 8%, and 11% concentration gelatin phantoms using a tone-burst generated by a piezoelectric actuator located on the solid surface. Attenuation profiles along depth and lateral axes are also calculated in order to probe some of the SAW properties described by Richart, et al.¹⁸ and Viktorov, et al.¹¹ Finally, a frequency test is conducted in the 8% phantom in order to demonstrate the inverse relationship between the effective penetration depth of Rayleigh waves and the excitation frequency.

2. THEORY

2.1 Rayleigh waves

This type of SAW propagates in a solid-vacuum interface. When the medium is assumed to be semi-infinite, isotropic, and homogeneous, Rayleigh waves propagate according to¹²

$$(\lambda + 2\mu)\nabla\nabla \cdot \vec{u} - \mu\nabla \times \nabla \times \vec{u} = \rho \frac{d^2\vec{u}}{dt^2} \quad (1)$$

where λ and μ are the Lamé coefficients of the medium, \vec{u} is the displacement, and ρ is the density of the medium. The solution of Eq. 1 using cylindrical coordinates leads to the Rayleigh wave dispersion equation given by¹²

$$4k_R^3\beta_R - (k_S^2 - 2k_R^2)^2 = 0 \quad (2)$$

where k_R is the Rayleigh wave number, k_S is the shear wave number, and $\beta_R = \sqrt{k_R^2 - k_S^2}$. The solution of Eq. 2 provides a relationship between shear wave speed c_S and Rayleigh wave speed c_R , which depends on the Poisson's ratio ν . Then, for $\nu = 0.5$ valid for incompressible materials like soft tissue, and assuming a linear elastic medium, this relationship is described by

$$c_R \approx 0.95c_S = 0.95 \sqrt{\frac{\mu}{\rho}} \quad (3)$$

According to Eq. 3, shear wave speed is faster than Rayleigh wave speed (95% of c_S) for a solid-vacuum interface and this relationship holds almost constant for a large range of materials. It is important to note that the particle motion amplitude of Rayleigh waves decays exponentially with depth as shown in the amplitude-depth plots calculated by Richart, et al.¹⁸ for different values of Poisson's ratio. Similarly, assuming that Rayleigh waves are generated by a point source acting in the solid-vacuum interface, a cylindrical wave-front will propagate through the solid boundary with an attenuation factor proportional to $1/\sqrt{r}$, where r is the distance from the point source.¹⁸ In contrast, body waves like shear waves attenuate at a rate of $1/r$ as described by the radiation condition in cylindrical waves. Finally, the effective penetration depth of Rayleigh waves is inversely proportional to the frequency f of the wave as described by¹¹

$$z \propto \lambda_R = \frac{c_R}{f} \quad (4)$$

where z is the effective penetration depth of the wave, and λ_R is the Rayleigh wave number.

2.2 Scholte waves

A Scholte wave is a type of SAW that propagates in a solid-fluid interface. Using the same assumptions of the medium as in the Rayleigh case, a dispersion equation can be derived:

$$4k_{Sc}^3\beta_{Sc} - (k_s^2 - 2k_{Sc}^2)^2 = k_{Sc}^4 \quad (5)$$

where k_{Sc} is the Scholte wave number, k_s is the shear wave number, and $\beta_{Sc} = \sqrt{k_{Sc}^2 - k_s^2}$. Note that Eq. 5 differs from Eq. 2 just in the last term. The solution of Eq. 5 provides a relationship between shear wave speed c_s and Scholte wave velocity c_{Sc} . Then, for $\nu = 0.5$, the relationship is described by

$$c_{Sc} \approx 0.839c_s = 0.839 \sqrt{\frac{\mu}{\rho}} \quad (6)$$

Then, the shear wave speed is faster than the Scholte wave speed (83.9% of c_s) for a solid-fluid interface.

3. MATERIALS AND METHODS

3.1 Sample preparation

Two tissue-mimicking phantoms were prepared by using 8% and 11% gelatin concentration, respectively, in order to create two differentiated mechanical properties (Young's modulus). Light scatterers were provided to the phantom by adding 2% concentration of intralipid powder. The dimensions of the phantom are approximately 15 x 7 x 3 cm embedded in a plastic container that enables the addition of water for the solid-fluid interface study (Figure 1a). The refractive index of the phantoms are approximately 1.35 in the visible spectrum which is close to real tissue.

The Young's modulus of each phantom was measured by conducting a stress-relaxation compressive test in three samples ($n = 3$) of each concentration using a MTS Q-Test/5 Universal Testing Machine (MTS, Eden Prairie, Minnesota, USA) with a 50 N load cell using a compression rate of 0.5mm/s, a strain value of 5% and total measurement time of 700s. A fractional derivative standard linear solid (FD-SLS) model¹⁹ was used to fit the stress-time plots in order to obtain frequency dependent Young's modulus. Finally, assuming an incompressible (Poisson's ratio of 0.5), homogenous, and isotropic medium, the calculated Young's modulus (E) is related to the shear wave speed (c_s) by

$$c_s = \sqrt{\frac{E}{3\rho}} \quad (7)$$

The shear wave speed for each phantom is estimated and used as a ground truth measurement in this study.

3.2 Experimental setup

PhS-OCT is implemented on a swept-source OCT system (HSL-2100-WR, Santec, Aichi, Japan) with a center wavelength of 1,318 nm and a full-width half-maximum (FWHM) bandwidth of 125 nm. The imaging depth was measured to be 5 mm (-10 dB sensitive fall-off). The optical lateral resolution is approximately 20 μm , and the FWHM of the axial point spread function after dispersion compensation is 10 μm . A galvo-scanner was used to change the lateral position of the beam in the sample. The synchronized control of the galvo-scanner and the OCT data acquisition was conducted using a LabView (Version 14.0f1, National Instruments Corporation, Austin, TX, USA) platform connected to a work station.

A needle attached to a piezoelectric actuator (APC 40-2020, APC International, Ltd., Macheyville, PA, USA) was located on the left side of the phantom as shown in Figure 1b. The actuator was connected to stereo amplifiers (LP-2020A+, Lepai, Houston, TX, USA) that receive harmonic signals from a dual channel function generator (AFG320, Tektronix, USA). The vibration of the needle generates SAW propagating from the left to the right side of the phantom. The OCT system enables the acquisition of motion frames within a region of interest (ROI) of 30 mm (lateral axis) x 2.5 mm (depth axis) as shown in Figure 1b.

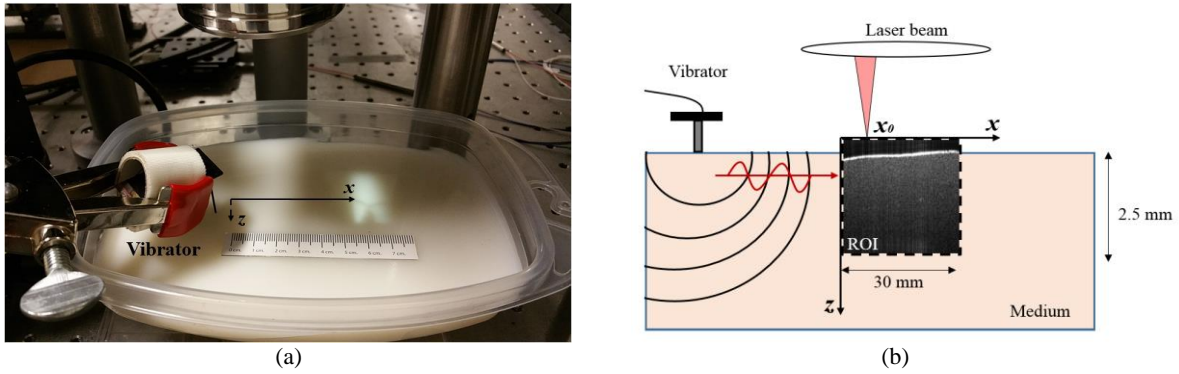


Figure 1 (a) Gelatin phantom embedded in a container. (b) Experimental setup showing a cross section of the phantom, location of vibrator, region of interest, and dimensions.

3.3 Tone-burst propagation (TBP) method

A harmonic source is used to create a tone-burst of a surface acoustic wave (SAW) propagating within the ROI of the phantom in two situations: solid-air, and solid-water interfaces. The tone is formed by four cycles of a harmonic wave of $f = 400$ Hz and $f = 1000$ Hz. The M-mode approach is used for generating space-time representations of the propagating wave. There is no communication between the function generator (which produces the tone-burst) and the OCT acquisition system; then, a synchronization approach is required (Figure 2). A tone is sent each 35 ms, and $M = 1400$ A-lines are scanned in $N = 400$ lateral positions. Then, the system is able to detect at least 2 tones in a single M-mode scanning, which requires 70 ms. The time given to the galvo-scanner for redirecting the beam between consecutive lateral positions is 35 ms in order to ensure the synchronization requirement.

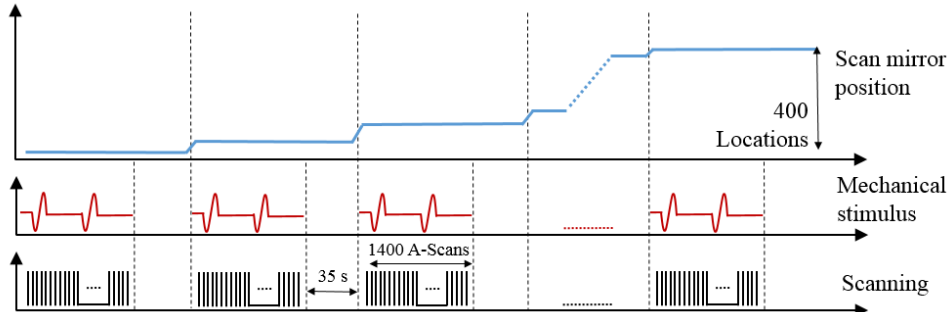


Figure 2 Acquisition protocol of TBP method using a PhS-OCT system.

Four hundred M-mode maps are acquired using the described protocol in order to cover the ROI lateral axis of 30mm. Figure 3a shows a B-mode structural OCT image of the ROI in a 11% gelatin phantom. A 2D M-mode map is formed using 1400 (time axis) x 1024 (depth axis) elements. We rearranged the scanning into a 3D volume of 400 x 1024 x 1400 elements in the lateral, axial, and time axes, respectively. 2D spatial motion frames can be obtained based on the 3D volume at a frame rate of 20 kHz (time resolution 50 μ s) as shown in Figure 3b. The propagation of the tone-burst can be represented as a 2D profile cut of the 3D volume at a given depth z which will provide 2D space-time maps. The SAW speed can be estimated by calculating the local slope of the pulse trajectory as

$$c_{SAW} = \frac{\Delta d_{SAW}}{\Delta t_{SAW}} \quad (8)$$

where Δd_{SAW} is the propagated distance of a transient SAW tone during time Δt_{SAW} .

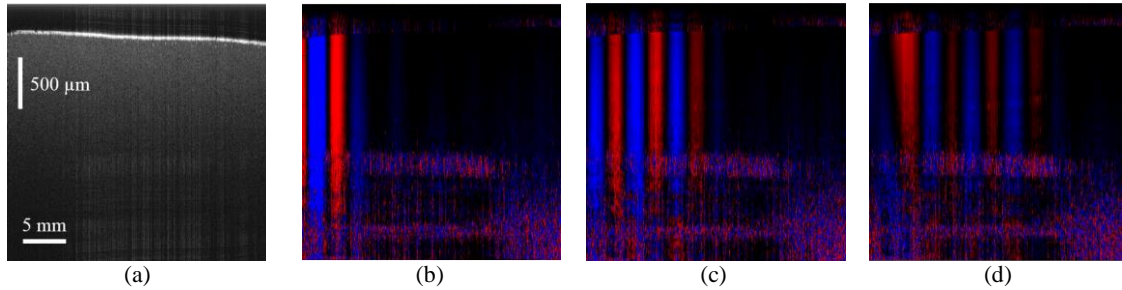


Figure 3 (a) B-mode OCT structural image of a 11% gelatin concentration phantom. (b) – (d) 2D motion frames at times 3 ms, 5 ms, and 7 ms, respectively, representing the Rayleigh wave propagation within the phantom in (a).

3.4 Experimental method

The main aim of this study is to demonstrate the presence of SAW propagating in two interfaces: solid-air, and solid-water. Phase velocities of Rayleigh and Scholte waves are measured in a 8% concentration gelatin phantom using a tone-burst of 1000 Hz, and in a 11% phantom using a 400 Hz tone-burst. Results generated by the mechanical test are used to estimate the shear wave speed for each phantom. Rayleigh-shear and Scholte-shear speed ratios are calculated and compared to theoretical findings. Attenuation profiles along depth and lateral axis are calculated in order to probe some of the SAW properties. Finally, a frequency test is conducted in the 8% phantom. Here, the vibration amplitude of Rayleigh waves at a given lateral and depth position of the phantom was calculated for 6 excitation frequencies of the tone-burst in a range of 400 Hz – 2000 Hz. The aim is to demonstrate the inverse relationship between the effective penetration depth of Rayleigh waves and the excitation frequency.

4. RESULTS

4.1 Mechanical measurements

Stress relaxation curves obtained with the compression test were fitted using a four-parameter FD-SLS model by using a non-linear constrained optimization approach for both phantom concentrations. Subsequently, shear wave speed versus excitation frequency was obtained by using the calculated parameters and a Fourier domain relationship described in Schmidt, et al.¹⁹ We found that the shear wave velocities in the 8% (1000 Hz excitation), and 11% (400 Hz excitation) concentration phantoms are 2.95 ± 0.10 m/s, and 4.84 ± 0.11 m/s, respectively.

4.2 Rayleigh and Scholte waves measurements

Space-time maps were obtained in the 8% and 11% concentration phantoms using the TBP method as shown in Figure 4a,b. Subsequently, the application of Eq. 8 to these maps enabled the calculation SAW-speed maps that represent the Rayleigh and Scholte wave speed for each lateral and depth position in a color-coded fashion (Figure 4c,e). The representative SAW speed for each phantom was calculated by applying a linear fitting in the propagation curve obtained by tracking the main peak of the tone-burst in space and time. For the 11% phantom, $c_R = 4.53$ m/s and $c_{Sc} = 3.87$ m/s were estimated as shown in Figure 4d. Using the mechanical test results, we found that $c_R/c_S = 93.6\%$, and $c_{Sc}/c_S = 80.0\%$. Similarly, for the 8% phantom, $c_R = 2.77$ m/s and $c_{Sc} = 2.43$ m/s were reported as shown in Figure 4f. Then, we calculated a $c_R/c_S = 93.9\%$, and $c_{Sc}/c_S = 82.4\%$.

Figure 5a shows the attenuation curves of the main peak of SAW when they propagate along the lateral axis. Curves attributed to an excitation frequency of 1000 Hz correspond to the 8% gelatin phantom, while those related to 400 Hz correspond to the 11% phantom. Attenuation curves were extracted in both situations: solid-air (Rayleigh waves), and solid-water (Scholte waves). Similarly, the attenuation of SAW vs. depth was reported in Figure 5b. Here, the depth axis was normalized by the wavelength for each case, and the vibration amplitude was divided by the vibration amplitude in the surface of the phantom as reported by Richart, et al.¹⁸ Finally, the vibration amplitude of a Rayleigh wave at a given lateral and depth position in the 8% concentration phantom was calculated for 6 excitation frequencies of the tone-burst in a range of 400 Hz – 2000 Hz and reported in Figure 6. Here, a rational function was fitted ($r^2 = 0.9919$) demonstrating the inverse relationship between frequency and effective penetration depth of Rayleigh waves.

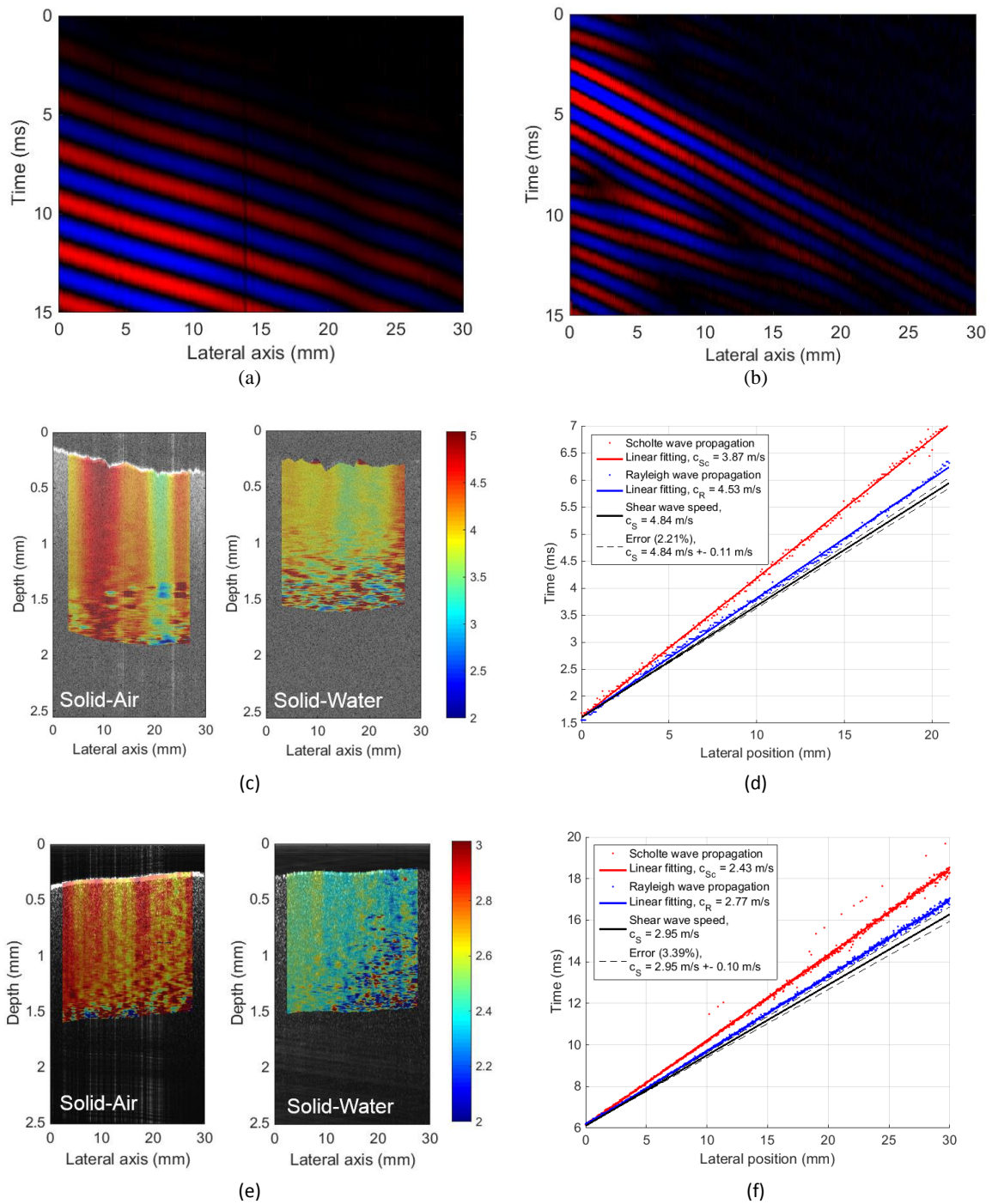


Figure 4 (a), (b) Space-time maps representing the propagation of Rayleigh waves in 11% (400 Hz) and 8% (1000 Hz) concentration phantoms, respectively at a given depth. (c), (d) 2D SAW speed maps, and speed comparison of SAW in solid-air and solid-water interfaces, respectively, for a 11% concentration phantom. (e), (f) 2D SAW speed maps, and speed comparison of SAW in solid-air and solid-water interfaces, respectively, for a 8% concentration phantom.

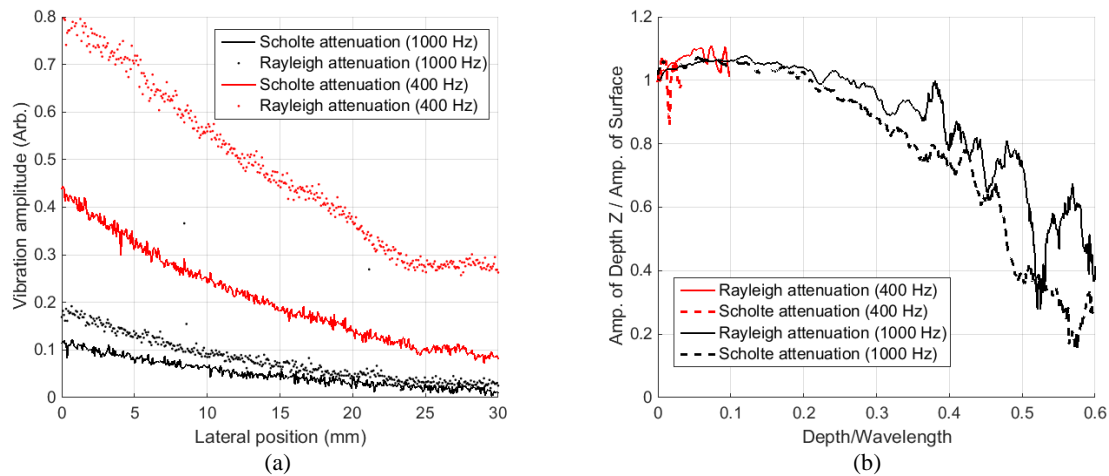


Figure 5 (a) Attenuation of SAW waves when they propagate along the lateral axis, and (b) attenuation vs. normalized depth in 11% (400 Hz), and 8% (1000 Hz) concentration phantoms in two boundary conditions: solid-air, and solid-water interfaces.

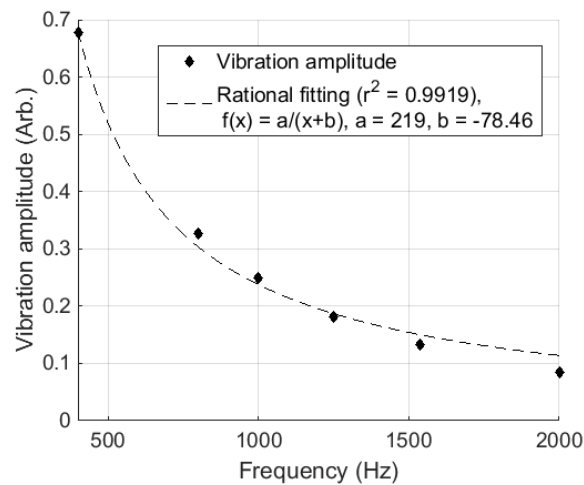


Figure 6 Inverse relationship between vibration amplitude of Rayleigh waves at a given lateral and depth position vs. excitation frequency in a 8% concentration phantom.

5. DISCUSSION AND CONCLUSIONS

Propagation of SAW in gelatin phantoms was demonstrated in this study under two conditions: semi-infinite solid-air, and solid-water media. Results confirm that Rayleigh waves propagate in solid-air interfaces with a phase speed ratio of 93.6% and 93.9% with respect to shear wave speed for 11% and 8% phantom concentrations, respectively, which is consistent to SAW theory (95%). Similarly, we found that Scholte waves propagate in solid-water interfaces at a speed ratio of 80.0% and 82.4% with respect to shear waves for both phantom concentrations, which is similar to theoretical findings (84%). SAW-speed maps shown in Figures 4c,d demonstrate that characterization of 2D mechanical properties of tissue using SAW and dynamic OCE is possible if the correct wave model is selected. Ignoring the presence of SAW and assuming shear wave propagation when the surface of the sample is mechanically excited could lead to non-trivial under-estimations of the phase speed, and, ultimately, in the miscalculation of the Young's modulus of the sample.

Attenuation curves (vibration amplitude vs. lateral axis) demonstrate an exponential decay tendency as expected in theory. Higher frequencies produce stronger attenuation as shown in Figure 5a. For all phantom concentrations, we found that Scholte waves have higher attenuation compared to Rayleigh waves, which is expected since water is a more dispersive medium. Figure 5b shows attenuation curves vs. normalized depth that are consistent with theoretical attenuation plots calculated by Richart, et al.¹⁸ for Rayleigh waves. Here, a higher frequency of 1000 Hz reduces the superficial zone in which the SAW propagates compared to the 400 Hz case. Finally, the inverse relationship between frequency and effective penetration depth of Rayleigh waves is demonstrated by a rational fitting ($r^2 = 0.9919$) in Figure 6.

In summary, the presence of SAW in gelatin elastic phantoms is demonstrated by producing a mechanical excitation in solid-air and solid-water interfaces using an OCT system. Phase speed, attenuation vs. lateral and depth axis, and attenuation vs. frequency were characterized when SAW were generated in 11% and 8% gelatin concentration phantoms. Experimental results confirm that Rayleigh waves propagate within solid-air interfaces, while Scholte waves propagate in solid-water interfaces. Future work will be focused in the study of SAW in real viscoelastic tissue such as lungs¹⁶, cornea¹⁷, and skin¹⁵.

ACKNOWLEDGEMENTS

The development of instrumentation required for this work was supported by the II-VI Foundation. Fernando Zvietcovich is supported by the Fulbright Program (U.S.A. Department of State), and Fondo para la Innovacion, la Ciencia y la Tecnologia FINCyT (Peruvian Government).

REFERENCES

- [1] Mulligan, J. A., Untracht, G. R., Chandrasekaran, S. N., Brown, C. N. and Adie, S. G., "Emerging Approaches for High-Resolution Imaging of Tissue Biomechanics With Optical Coherence Elastography," *Selected Topics in Quantum Electronics*, IEEE Journal of 22(3), 1-20 (2016).
- [2] Sandrin, L., Fourquet, B., Hasquenoph, J.-M., Yon, S., Fournier, C., Mal, F., Christidis, C., Ziol, M., Poulet, B., Kazemi, F., Beaugrand, M. and Palau, R., "Transient elastography: a new noninvasive method for assessment of hepatic fibrosis," *Ultrasound in Medicine & Biology* 29(12), 1705-1713 (2003).
- [3] Schmitt, C., Soulez, G., Maurice, R. L., Giroux, M. F. and Cloutier, G., "Noninvasive Vascular Elastography: Toward A Complementary Characterization Tool of Atherosclerosis in Carotid Arteries," *Ultrasound in Medicine & Biology* 33(12), 1841-1858 (2007).
- [4] Donald, B. P., Jonathan, B., Abbas, S. and Justin, S., "Visualization and quantification of breast cancer biomechanical properties with magnetic resonance elastography," *Physics in Medicine and Biology* 45(6), 1591 (2000).
- [5] Detorakis, E.T. and Pallikaris, I. G., "Ocular rigidity: biomechanical role, in vivo measurements and clinical significance," *Clinical & Experimental Ophthalmology* 41(1), 73-81 (2013).
- [6] Parker, K. J., Doyley, M. M. and Rubens, D. J., "Imaging the elastic properties of tissue: the 20 year perspective," *Physics in Medicine and Biology* 56(1), R1 (2011).
- [7] Muthupillai R., Lomas, D. J., Rossman, P. J., Greenleaf, J. F., Manduca, A. and Ehman, R. L., "Magnetic resonance elastography by direct visualization of propagating acoustic strain waves," *Science* 269(5232), 1854-1857 (1995).
- [8] Wang, S. and Larin, K. V., "Optical coherence elastography for tissue characterization: a review," *Journal of Biophotonics* 8(4), 279-302 (2015).
- [9] Li, C., Guan, G., Reif, R., Huang, Z. and Wang, R. K., "Determining elastic properties of skin by measuring surface waves from an impulse mechanical stimulus using phase-sensitive optical coherence tomography," *Journal of The Royal Society Interface* 9(70), 831-841 (2012).
- [10] Graff, K. F., [Wave Motion in Elastic Solids], Dover Publications, New York, 273-393 (2012).
- [11] Viktorov, I. A., [Rayleigh and Lamb waves: physical theory and applications], Plenum Press, New York, 1-6 (1967).

- [12] Nenadic, I. Z., Urban, M. W., Bernal, M. and Greenleaf, J. F., "Phase velocities and attenuations of shear, Lamb, and Rayleigh waves in plate-like tissues submerged in a fluid (L)," *J Acoust Soc Am* 130(6), 3549-3552 (2011).
- [13] Mercado, K. P., Langdon, J., Helguera, M., McAleavey, S. A., Hocking, D. C. and Dalecki, D., "Scholte wave generation during single tracking location shear wave elasticity imaging of engineered tissues," *J Acoust Soc Am* 138(2), EL138-EL144 (2015).
- [14] Li, C., Guan, G., Huang, Z., Wang, R. K. and Nabi, G., "Full skin quantitative optical coherence elastography achieved by combining vibration and surface acoustic wave methods," *Proc. SPIE* 9322, 93220O-1 – 93220O-9 (2015).
- [15] Zhang, X., Osborn, T. G., Pittelkow, M. R., Qiang, B., Kinnick, R. R. and Greenleaf, J. F., "Quantitative assessment of scleroderma by surface wave technique," *Medical Engineering and Physics* 33(1), 31-37 (2011).
- [16] Zhang, X., Qiang, B., Hubmayr, R. D., Urban, M. W., Kinnick, R. and Greenleaf, J. F., "Noninvasive ultrasound image guided surface wave method for measuring the wave speed and estimating the elasticity of lungs: A feasibility study," *Ultrasonics* 51(3), 289-295 (2011).
- [17] Wang, S. and Larin, K. V., "Noncontact depth-resolved micro-scale optical coherence elastography of the cornea," *Biomedical Optics Express* 5(11), 3807-3821 (2014).
- [18] Richart, F. E., Hall, J. R. and Woods, R. D., [Vibrations of soils and foundations], Prentice-Hall, New Jersey 191-235 (1970).
- [19] Schmidt, A. and Gaul, L., "Experimental Investigation and Numerical Treatment of Viscoelastic Materials," *Proceedings of the International Model Analysis Confernece* 3(1), 1557-1566 (2008).